electronics

MDPI

Article

A Stacked Substrate-Integrated Waveguide-Based Pyramidal Horn Antenna for Terahertz Communications

Biswash Paudel *, Xue Jun Li * and Boon-Chong Seet

Department of Electrical and Electronic Engineering, Auckland University of Technology, Auckland 1010, New Zealand; boon-chong.seet@aut.ac.nz

* Correspondence: biswash.paudel@autuni.ac.nz (B.P.); xuejun.li@aut.ac.nz (X.J.L.)

Abstract

The terahertz (THz) band offers ultra-wide bandwidth for next-generation high-speed wireless communication systems. However, achieving compact, high-gain, and beam-symmetric THz antennas remains challenging due to fabrication and propagation constraints. This paper presents a simulation-based design and optimization of a stacked substrate-integrated waveguide (SIW) pyramidal horn antenna achieving equal half-power beamwidths (HPBWs) in both E- and H-planes. The design employs vertically stacked SIW layers coupled through optimized slot apertures to ensure dominant TE_{10} mode propagation with minimal reflection. Using full-wave electromagnetic simulations, the effects of layer number, dielectric loading, amplitude tapering, and phase distribution are systematically analyzed. The optimized five-layer configuration exhibits 10 dBi gain, 41° HPBW, and sidelobe levels around −3.2 dB at 210 GHz. This framework aims to develop high-performance, beam-symmetric THz SIW antennas compatible with standard LTCC/PCB technologies.

Keywords: terahertz band; horn antenna; substrate-integrated waveguide; beam symmetry; multi-layered

Academic Editors: Muhammad Usman Hadi and Muhammad Ikram Ashraf

Received: 10 November 2025
Revised: 28 November 2025
Accepted: 2 December 2025
Published: 4 December 2025

Citation: Paudel, B.; Li, X.J.; Seet, B.-C. A Stacked Substrate-Integrated Waveguide-Based Pyramidal Horn Antenna for Terahertz Communications. *Electronics* **2025**, *14*, 4780. https://doi.org/10.3390/electronics14234780

1. Introduction

The exponential growth of data traffic, driven by emerging applications such as high-definition video streaming, autonomous vehicles, the Internet of Things (IoT), and real-time online gaming, is accelerating the demand for higher bandwidth, lower latency, and enhanced signal reliability, pushing wireless communication towards the terahertz (THz) spectrum [1]. While the THz band offers unprecedented potential for ultra-high-speed wireless communication, designing antennas that are compact, high-gain, and beam-symmetric at these frequencies remains challenging due to fabrication constraints and significant propagation losses. Addressing these challenges requires innovative design strategies that balance performance, manufacturability, and integration into next-generation communication systems. This necessitates the development of THz communication antenna systems that combine efficiency, compactness, and high gain [2]. Miniaturization is a crucial requirement for THz antenna systems, enabling compact and planar circuit integration. Rectangular horn antennas are widely favored among different antenna designs because of their high gain, wide bandwidth, strong power handling, and straightforward structural design. However, their bulky flared waveguide structure makes integration with planar monolithic microwave circuits (MMICs) difficult, leading to increased fabrication complexity, especially at THz frequencies [3–6].

To address these limitations, Substrate-Integrated Waveguide (SIW) technology has emerged as an effective solution. SIW is a planar form of rectangular waveguide (RWG) that combines low loss, high quality factor, compact size, and simple fabrication while maintaining the essential properties of its dominant mode [7]. SIW-based horn antennas offer a lightweight structure with strong compatibility to planar fabrication technologies, and they can be effectively excited through mode transition or aperture coupling techniques [8,9]. These attributes make SIW horn antennas especially appealing for THz applications, where seamless integration with other planar components is essential; however, realizing compact, high-gain, and beam-symmetric designs at such frequencies remains a significant challenge.

In addition, performance enhancements can be achieved through dielectric loading techniques [6]. For SIW horn antennas, periodically perforating the substrate with sub-wavelength hole arrays enables precise tuning of the effective permittivity, thereby improving impedance matching and radiation efficiency [2]. Beam symmetry and bandwidth performance can also be matched with an extended parallel-plate structure [10].

Building on these advances, this paper introduces a stacked SIW horn antenna architecture with optimized slot transitions and aperture field control, aimed at achieving high gain, beam symmetry with equal half-power beam-width (HBPW) in both E- and H-planes, and compact integration suitable for next-generation THz communication systems. This is accomplished through five layers of SIW horn antennas and feeding through a single port, allowing for consistent excitation of each antenna layer by distributing the signal via the etched slot. Although the proposed antenna employs multiple stacked SIW layers and a feeding network, its fabrication remains relatively simple because each section is realized using standard planar SIW processing techniques such as via drilling and slot etching. Unlike conventional metallic horn or corrugated structures requiring precision machining, the entire design is compatible with PCB and low-temperature co-fired ceramic (LTCC) technologies, ensuring ease of mass production at THz frequencies. The remainder of the paper is organized as follows: Section 2 reviews related work; Section 3 presents the proposed antenna geometry; Section 4 describes the stacked-layer SIW power splitter; and Section 5 discusses the antenna performance when fed by the proposed network. Finally, Section 6 summarizes the key findings and concludes the paper.

2. Related Works

Extensive research has investigated different horn antenna configurations for THz applications. While stepped and corrugated horn designs have been introduced to enhance gain and bandwidth, their complex geometry poses significant challenges for seamless integration into planar THz systems and hinders scalable fabrication. To address these limitations, SIW horn antennas have emerged as a more practical solution, offering compactness, ease of fabrication, and compatibility with planar integration.

A 2×2 SIW horn antenna was proposed in [5] using vertical and horizontal power splitters. Despite its high gain, it exhibited asymmetrical E- and H-plane HPBWs and elevated sidelobe levels (SLLs). The performance of SIW horn antennas may be compromised by the use of thin substrates. While thin substrates are favoured for compact designs, they can cause degraded radiation patterns, narrower bandwidth, and impedance mismatches with free space. A multilayer SIW power divider (1×4 and 1×8) was proposed in [11], utilizing only two substrate layers. The authors employed a 2D power-division scheme in one plane, followed by slot coupling into other layers to further divide the signal into four or eight outputs. Similarly, a two-layer stacked SIW-to-SIW transition operating in the sub-THz band was introduced in [1], using a rectangular slot to transfer EM waves between layers, forming a vertical waveguide-like structure. However, this approach requires through-hole structures and gold bumps to achieve the desired E-field distribution.

An eight-layer SIW stacked power divider for SIW-to-RWG transition was presented in [12], utilizing a wedge transition for sub-THz frequencies. However, the design did not consider feeding the divider into the antenna array and exhibited limited bandwidth. Ettorre et al. [13] proposed a multi-beam leaky-wave antenna using stacked substrate layers, with horn antennas in one layer and radiating slots in another, coupled through the parabolic surface of a quasi-optical system. Wang et al. [14] employed a multilayer structure in their composite FHMSIW/SSPP waveguide, using upper, middle, and lower copper layers connected via through and blind vias. The lower layers were modulated to achieve continuous beam scanning, while the upper layer provided feeding and unidirectional radiation. This multilayer approach enables compact field confinement, slow-wave propagation, and effective mode conversion across the stacked layers. Liang et al. [2] presented an all-silicon 2-D planar horn antenna operating from 220 to 330 GHz (WR-3). The design uses a sub-wavelength hole lattice to form an effective-medium silicon platform and integrates a 2-D dielectric lens for wavefront flattening and improved free-space matching, achieving a compact footprint with ∼11–15 dBi realized gain (fabricated via deep reactive ion etching). In contrast, our work targets 210 GHz and employs a stacked SIW horn fed by a slot-coupled multilayer SIW power splitter engineered to realize Gaussian amplitude with near-uniform phase $\Delta\phi \approx 0^\circ$ across five layers, explicitly aiming for equal HPBWs in the E- and H-planes using PCB/LTCC-compatible SIW processes (vias and etched slots) and no external dielectric lens.

As aforementioned, much prior RF/THz antenna work targets lower bands due to the fabrication complexity, material losses, and measurement difficulty at higher frequencies. Despite steady progress, SIW-based multilayer power splitters at sub-THz/THz remain relatively scarce, motivating innovative, compact feeding networks that preserve mode purity and aperture phase coherence. This paper addresses this gap with a simple, slot-coupled multilayer SIW divider feeding a stacked SIW horn, achieving symmetric HPBWs and ≈10 dBi simulated gain at 210 GHz, while maintaining planar manufacturability and MMIC integration compatibility.

3. Design of SIW THz Horn Antenna

3.1. Design Rationale and Methodology

The aperture field distribution of a horn antenna strongly impacts its HPBW, directivity, SLLs, and front-to-back ratio (FTBR). Achieving equal HPBW in both planes yields tangible advantages for THz system design. Symmetric beamwidth mitigates beam ellipticity, resulting in more predictable link budgets, improved beam acquisition efficiency, and reduced sensitivity to mechanical misalignment. These factors become increasingly critical at THz frequencies due to narrow beams and significant atmospheric attenuation [15]. In beam-steered THz ISAC and MIMO architectures, matching the E- and H-plane HPBW also helps minimize angular distortion, enhances spatial resolution uniformity, and streamlines digital beamforming calibration [16,17]. Consequently, E- and H-plane beam symmetry serves not only as an electromagnetic optimization criterion but also as a key requirement for ensuring stable and high-performance operation in THz communication and sensing systems.

To enable compact and high-performance THz components, multi-layered technologies have gained significant interest. In a single-layer SIW-based antenna, the feeding structure often occupies a large footprint, limiting design flexibility. Conversely, stacked multilayer configurations allow the transformation of a 2D planar structure into a compact 3D structure, offering enhanced integration and miniaturization, especially at THz frequencies [2,13,18,19]. The proposed design employs multiple vertically stacked SIW horn antenna layers, with the common metal layers between adjacent horns removed to create a continuous E-plane aperture. The number of layers directly influences the beamwidth;

however, increasing layers can introduce aperture phase errors, degrading gain and radiation performance despite a larger physical aperture [20]. To mitigate these phase distortions and maintain flare uniformity, careful optimization of the number of layers and flare geometry was performed using Ansys HFSS full-wave simulations. This ensures the balanced performance across both radiation planes while maintaining a compact form factor suitable for the integrated THz front-end systems.

3.2. Antenna Geometry

The proposed antenna consists of a five-layer stacked dielectric-loaded SIW H-plane horn structure, excited by a five-port TE_{10} mode feeding network. The antenna is designed to operate at a center frequency of 210 GHz. The geometric configuration is illustrated in Figure 1, and the detailed dimensions, optimized according to standard SIW design principles [21], are listed in Table 1. These parameters were chosen to minimize leakage and ensure optimal performance at the target frequency.

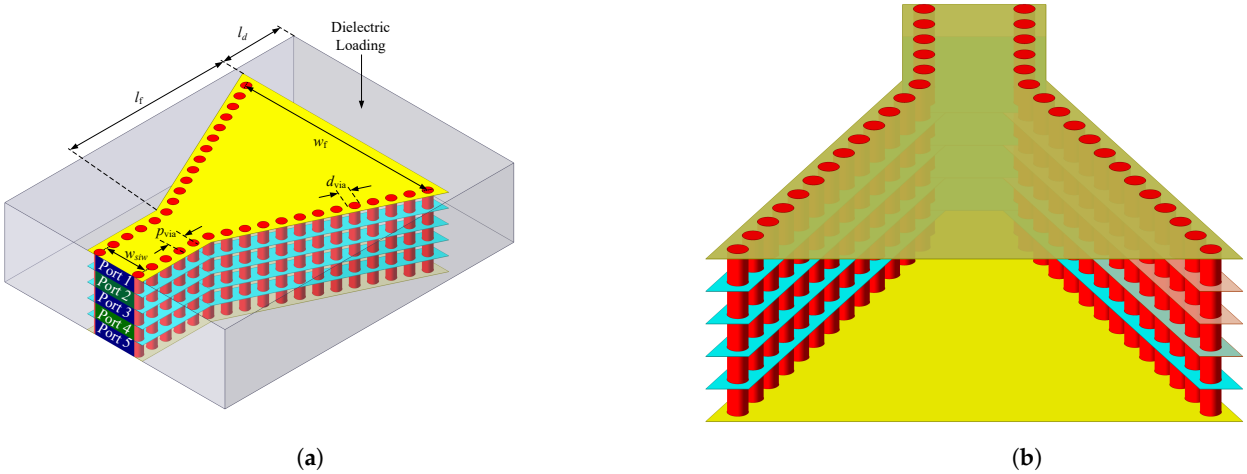

(**a**) (**b**)

Figure 1. Structural layout of the proposed SIW horn antenna: (**a**) Isometric view and (**b**) Sectional view showing the metal layer and via holes.

Each layer is fabricated on a polyimide substrate with a dielectric constant (ϵ_r) of 3.5, a loss tangent (tan δ) of 0.008, and a total thickness of 1.25 mm. The flare angle in the H-plane is set to 60° to provide an optimal balance between directivity and compactness. Due to manufacturing constraints, implementing a flare in the E-plane is challenging at such high frequencies. To overcome this, the proposed design utilizes vertical stacking of SIW horns to mimic an E-plane flared aperture, thereby achieving near-symmetric beam widths without complex fabrication steps.

The five vertically stacked SIW H-plane apertures behave as a short broadside array of identical sub-apertures. With broadside (in-phase) excitation and identical flare/path length, the total radiation can be viewed as the element pattern multiplied by a vertical array factor [22]. As the effective aperture height increases, the beam in the stacking direction narrows (beamwidth $\propto \lambda$/height), which promotes E/H beamwidth symmetry as height approaches width [23]. To avoid the grating lobes (or efficiency loss where they appear), inter-layer spacing should remain sub-wavelength, since grating lobes steal power and reduce aperture efficiency/directivity [24]. Finally, a gentle amplitude tapering across layers (Gaussian distribution) suppresses the sidelobe at the cost of a small main-beam widening.

Table 1. Parameters of the SIW horn antenna (unit: mm).

w_{SIW}	0.65	w_f	5.65
l_f	3.9	p_{via}	0.25
l_d	1.25	d_{via}	0.15

3.3. Simulation Results

The simulation is performed using a lossy dielectric substrate (polyimide) and metallic layers (copper). The E- and H-plane gains, simulated with uniform magnitude and phase excitation at each port, are shown in Figure 2.

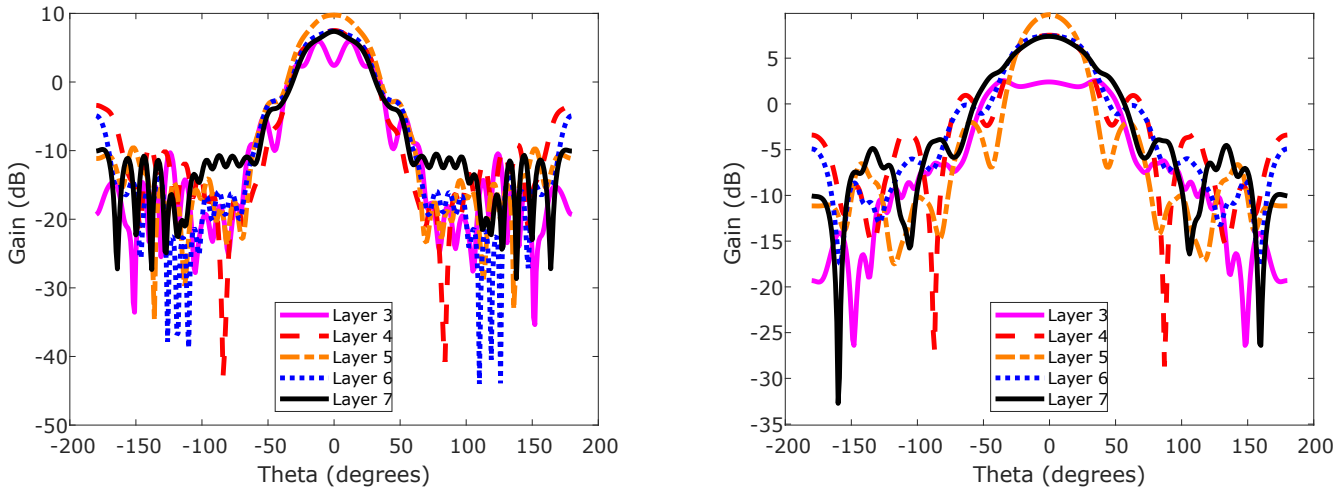

Figure 2. Simulated radiation gain at 210 GHz with varying number of SIW layers with uniform magnitude and phase for all the ports: (**a**) E-plane; (**b**) H-plane.

To comprehensively analyze the scaling behavior, the number of stacked SIW layers was varied from three to seven. As expected, the gain initially increases with aperture height, with the 5-layer configuration exhibiting the highest value. However, a noticeable drop occurs when increasing from five to six layers, and the 7-layer case shows a similar gain level to the six-layer design, indicating that the performance saturates beyond five layers.

This behavior arises from aperture phase imbalance rather than simulation limitations. Under uniform excitation (identical amplitude and phase at each port), the additional layers slightly disturb inter-layer phase coherence, producing partial field cancellation at the aperture and a modest reduction in effective radiation efficiency. At 210 GHz, the thicker stack also introduces higher dielectric and conductor losses, further limiting gain improvement.

The E- and H-plane gains in Figure 3 rise with the dielectric length up to an optimum near $l_d = 1.25$ mm, after which performance degrades. We size l_d on the order of the guided wavelength λ_g in the loaded region and then fine-tune it at 210 GHz, giving $l_d \approx 1.2\lambda_g$. Physically, shorter l_d under-corrects the aperture phase (i.e., wider H-plane beam), whereas longer l_d over-lenses the aperture and adds dielectric loss/phase non-uniformity, broadening the H-plane lobe and reducing gain. This behavior matches established SIW H-plane horn observations [25].

The input ports of our SIW horn antenna, labeled Port 1 to Port 5 as shown in Figure 1a, are each excited in the TE_{10} mode, with either uniform (identical amplitude and phase) or non-uniform (different amplitude and/or phase) excitations. To improve the radiation characteristics of the stacked SIW horn antenna, a Gaussian amplitude excitation pro-

file [26] is applied across the feeding ports. Gaussian excitation port generates a tapered field distribution that more closely approximates ideal aperture illumination, a technique commonly employed to suppress side lobes, improve beam symmetry, and enhance directivity, particularly important for THz-band antennas, where the physical aperture size is inherently limited.

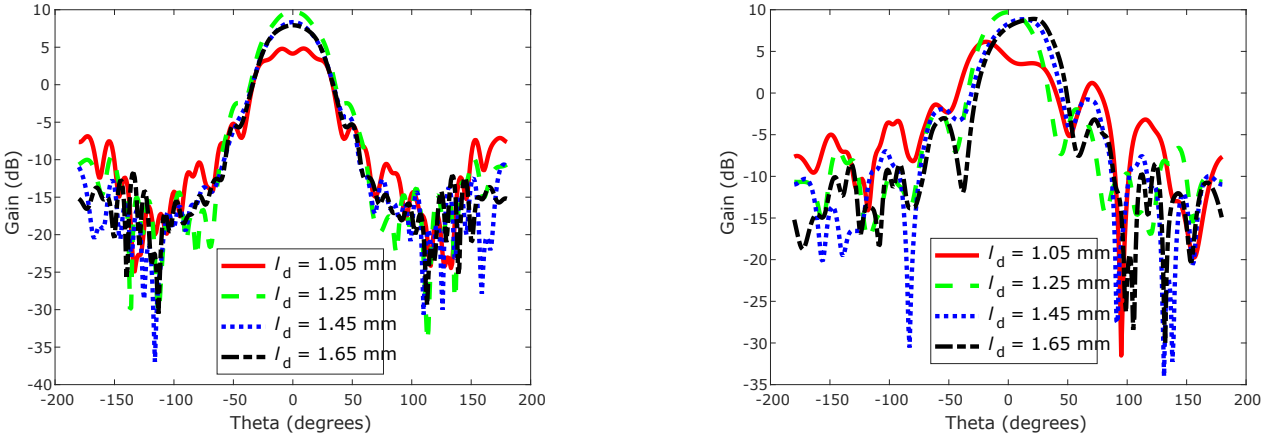

Figure 3. Simulated radiation gain for a 5-layer at 210 GHz with varying dielectric loading lengths with uniform magnitude and phase: (**a**) E-plane; (**b**) H-plane.

The excitation amplitude of each port is computed using the Gaussian function:

$$A(n) = A_0 e^{-\frac{(n-c)^2}{2\sigma^2}}, n = 1, 2, 3, \ldots, N \quad (1)$$

where $A(n)$ is the amplitude of the n-th port; $A_0 = 1$ is the peak amplitude at the center port; $c = 3$ is the center index for our 5-layer stacked SIW horns antenna; σ is the control factor for the taper sharpness (or standard deviation); and $N = 5$ is the total number of layer or ports. To evaluate the effects of the taper, σ was varied from 1.0 to 1.3 with a step size of 0.1. The H-plane was found to be strongly affected by the choice of σ. For $\sigma \leq 1.1$, the taper becomes too narrow, significantly reducing excitation at the outer ports. This effectively decreases the vertical aperture height, resulting in a wider H-plane beam and reduced gain as seen in Figure 4b. Similarly, when a $\sigma \geq 1.3$, the aperture becomes too broad, increasing outer-port illumination and again producing a broader H-plane main lobe with lower peak gain due to non-uniform aperture fields.

In contrast, the E-plane radiation pattern is mostly unaffected by variations in σ as shown in Figure 4a. This is because the E-plane beamwidth is governed mainly by the horizontal flare geometry rather than the vertical amplitude taper, making it far less sensitive to σ-dependent variations [3]. Among all tested values, $\sigma = 1.2$ provides the most balanced aperture illumination yielding, the narrowest H-plane beam and the highest gain.

To further analyze the effect of phase variation across the five feeding ports, four sets were applied:

- Set A: uniform phase (i.e., 0° phase at all ports)
- Set B: $+30^\circ$, $+15^\circ$, 0°, -15°, -30°
- Set C: $+60^\circ$, $+30^\circ$, 0°, -30°, -60°
- Set D: $+90^\circ$, $+45^\circ$, 0°, -45°, -90°

These patterns are symmetric about the center port (Port 3), while preserving the boresight direction in the ideal case, with phase gradient magnitude increasing from A to D. This variation lets us systematically probe the sensitivity of beam symmetry, HPBW, and SLLs to phase imbalance without steering the beam.

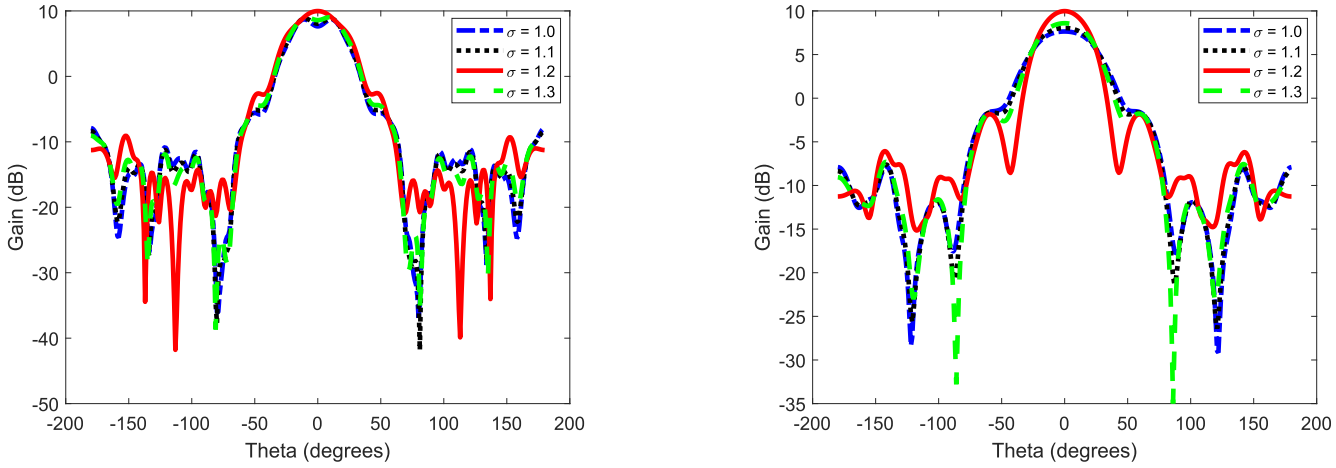

(**a**) (**b**)

Figure 4. Simulated radiation gain at 210 GHz with varying excitation magnitude (**a**) E-plane (**b**) H-plane.

Simulation results in Figure 5 indicate that uniform phase excitation yields constructive interference of the emitted waves in the end-fire direction, thereby enhancing both directivity and symmetry of the radiation pattern. This behavior aligns with antenna array theory [27], where uniform phase maximizes coherent addition in the desired look direction. Conversely, introducing a phase disrupts the aperture field distribution, distorting the main lobe and raising SLLs, ultimately degrading the performance in both E- and H-plane.

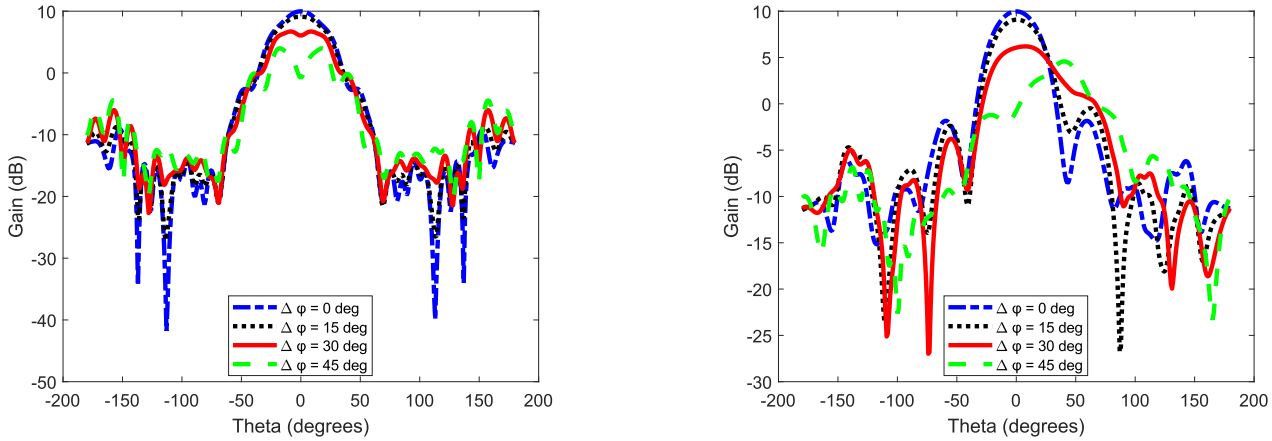

(**a**) (**b**)

Figure 5. Simulated radiation gain at 210 GHz with varying Phase difference while keeping $\sigma = 1.2$ (**a**) E-plane (**b**) H-plane.

The performance results for HPBW versus frequency are shown in Figure 6a, where the variation between the E- and H-planes arises from the aperture geometry of the stacked SIW horn. Specifically, the smaller effective aperture dimension in the E-plane generally produces a wider HPBW compared to the H-plane [27]. At 210 GHz, the combined use of a Gaussian amplitude distribution and uniform phase excitation produces more uniform aperture illumination. This approach effectively balances the field distribution in both principal planes, yielding equal HPBW of 41°. Detailed peak gain plots versus antenna design parameters are provided in Appendix A.

Similarly, the SLLs presented in Figure 6b are relatively consistent across both planes. The proposed SIW stacked pyramidal horn antenna achieves an SLL of approximately

−3.1 dB, which reflects the design trade-off made to prioritize planar configuration and equal HBPW over SLL suppression.

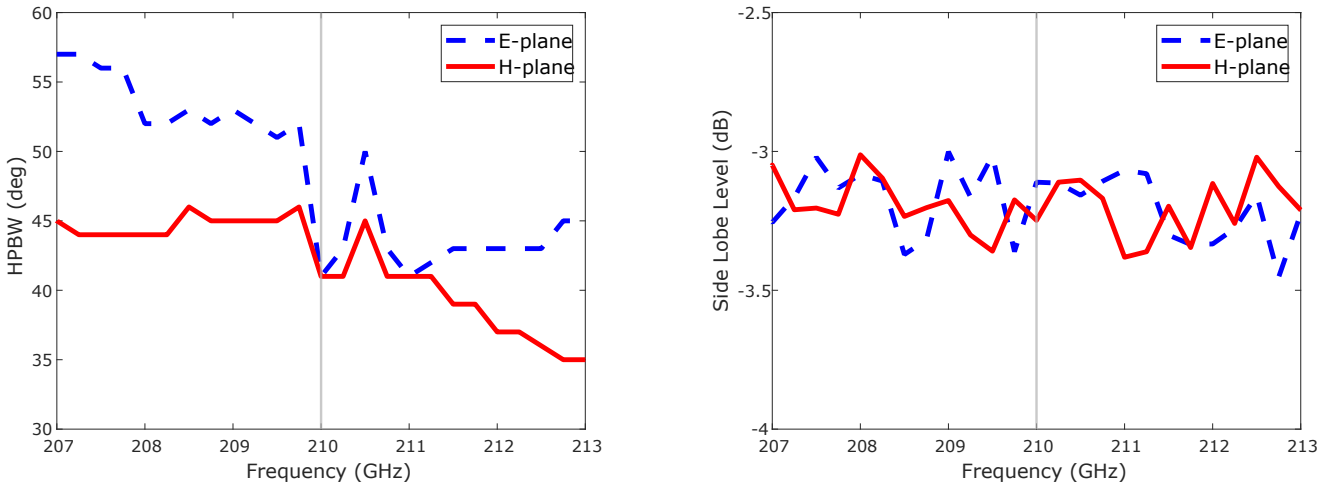

(**a**) (**b**)

Figure 6. Performance summary of the simulated SIW stacked horn antenna for $\sigma = 1.2$ and $\Delta\phi = 0°$ (**a**) HPBW (**b**) SLL.

As illustrated in Figure 7a, tuning both magnitude and phase across the target frequency range results in FTBR variations of approximately 10 dB, while achieving a peak gain of 10 dB. Optimal performance occurs at 210 GHz, as demonstrated in Figure 7b. In practical implementations, maintaining constant input phase and magnitude across wide bandwidths proves challenging. However, by independently adjusting these parameters at each frequency point, the radiation characteristics can be precisely optimized.

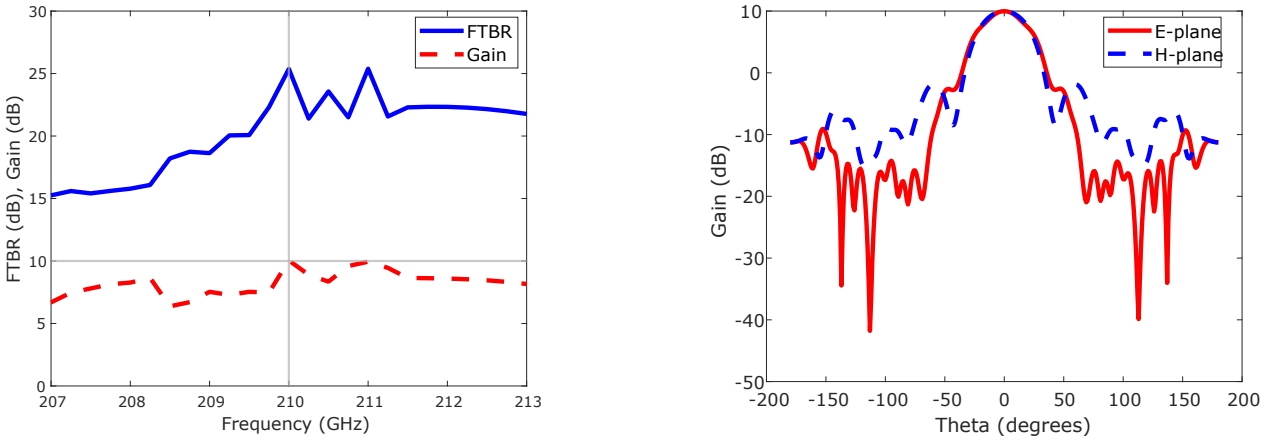

(**a**) (**b**)

Figure 7. Simulated performance of SIW stacked antenna for for $\sigma = 1.2$ and $\Delta\phi = 0°$ (**a**) FTBR and gain (**b**) Gain in E- and H-plane at 210 GHz.

Using the obtained excitation magnitude ($\sigma = 1.2$) and uniform phase, the electric field (E-field) distribution is illustrated in two cuts: the H-plane shown in Figure 8a, corresponding to a standard H-plane SIW horn antenna, and the E-plane, shown in Figure 8b. In the E-plane, the uniform phase across all five input TE_{10} ports results in field coupling beginning at the location where the adjacent metallic layer of the horn is removed. Along the propagation direction, the field intensity gradually decreases due to energy spreading across the flared region of the horn. Towards the end, the dielectric loading functions as a lens, focusing energy into the end-fire direction, and a similar effect is observed in the H-plane [3].

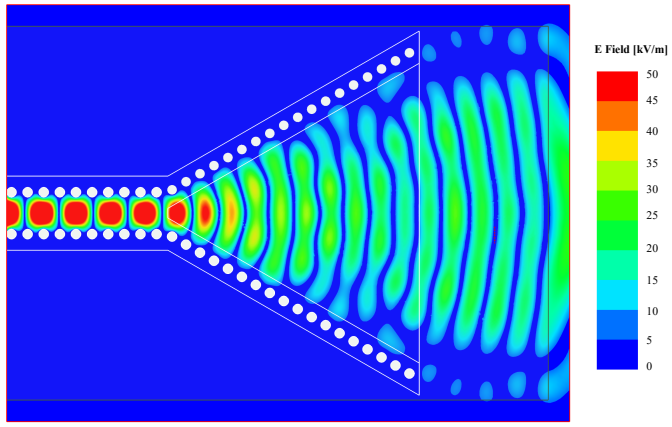

(**a**)

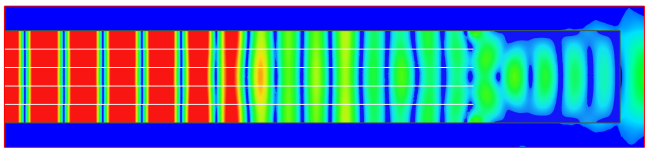

(**b**)

Figure 8. Simulated E-field plots at 210 GHz when $\sigma = 1.2$ and $\Delta\phi = 0^\circ$ (**a**) H-plane along the center axis and (**b**) E-plane along the center axis.

4. Stacked-Layer SIW Feeding Network

The proposed SIW-based horn antenna requires excitation of five stacked ports in the pure TE_{10} mode, with a magnitude following a Gaussian excitation profile ($\sigma = 1.2$) and uniform phase at 210 GHz. Any deviation from these conditions results in degraded antenna performance. To transfer EM energy through the multiple layers of the SIW horn antenna, a coupling transition is realized using a rectangular slot ($l_{slot} \times w_{slot}$) etched into the metallic layer of the feeding SIW. In addition, a metallic block acting as a shirt circuit is employed to suppress EM leakage into undesired directions [18,19].

The characteristic impedance of a single port (Z_{sp}) in the SIW feeding network is expressed as:

$$Z_{\text{sp}} = \frac{\pi h_{\text{sub}}}{2w_{\text{eqv}}} \cdot \frac{120\pi}{\sqrt{\epsilon_r}\sqrt{1-\left(\frac{\lambda_g}{2w_{\text{eqv}}}\right)^2}} \tag{2}$$

where h_{sub} is the single-port substrate thickness; w_{eqv} is the equivalent SIW port width [28]; λ is the guided wavelength and ϵ_r is the dielectric constant of the substrate material in the splitter network. For a multilayer SIW power splitter, the combined impedance Z_{c} is given by:

$$Z_{\text{c}} = \frac{Z_{\text{sp}}}{N} \tag{3}$$

where N is the number of stacked SIW layers.

Figure 9 illustrates the proposed five-layer SIW power splitter geometry and its equivalent topology with axis convention adopted throughout this work: x is the stacking (thickness) axis, y is the SIW width axis, and z direction is the longitudinal (propagation) axis. The input Port 6 excites the SIW in TE_{10} and propagates along the z through section [a–b] ($1 \rightarrow 3$) followed by [a–c] ($1 \rightarrow 2$). Slot I and Slot II (each $l_{\text{slot}} \times w_{\text{slot}}$) are etched in the common metal planes between layers and oriented with their one side along y (transverse

to z), which places the slot across the $TE_{10}E_y$ maxima and couples power along x into adjacent SIW layers with high mode purity.

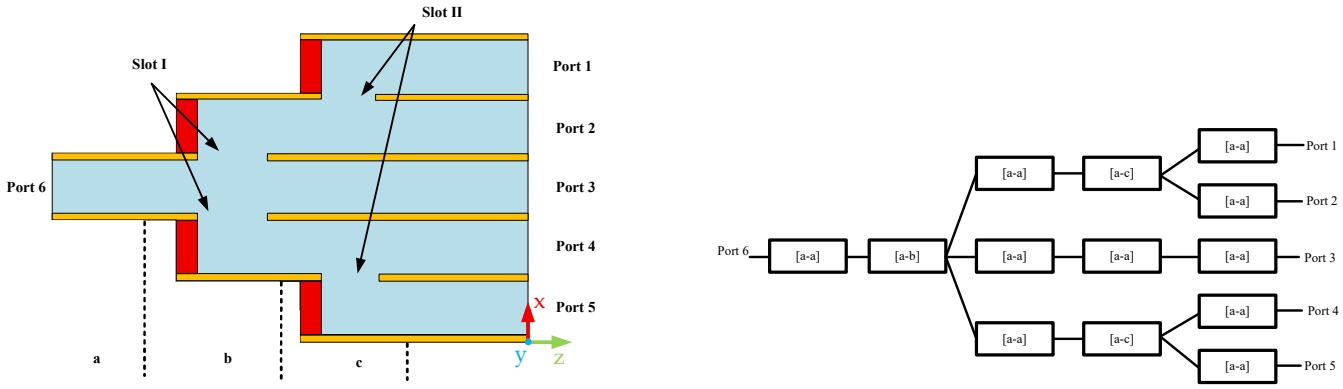

(**a**) (**b**)

Figure 9. Layout of the designed five-way power divider (**a**) Lateral view of the proposed power splitter and (**b**) Simplified layout based on recurring section

Full-wave EM simulations were used to size the slots ($l_{\text{slot}} \times w_{\text{slot}}$) and set their placement to achieve efficient power splitting with minimal reflection. Each splitting interface was tuned for < -10 dB at 210 GHz, ensuring excitation of only the dominant TE_{10} mode in all layers. With the optimized geometry, impedance mismatch is small and the inter-port phase spread at the outputs is within a few degrees, preserving mode purity throughout the multilayer network.

Port 6 excites a single SIW layer in TE_{10} (section [a–a]). The subsequent section [a–b] performs a $1 \rightarrow 3$ split across the stacked layers, after which [a-a] is reused and followed by [a–c] to realize $1 \rightarrow 2$ split. In this notion, [a–a] denotes a one-layer through section, while [a–b] and [a–c] are power division sections; their detailed layouts and field distributions are described below.

4.1. [a–b] Section

The *a–b* section serves as the initial splitter of the feeding port and is a critical component of the SIW power splitter. It enables the transition of electromagnetic (EM) power from a single-layer SIW structure to a three-layer configuration. Figure 10a presents the isometric view of the *a–b* splitter, with the outer shell omitted for clarity. A rectangular slot is etched into the inner layers to guide the EM energy into the three layers. To ensure propagation in the desired direction, a central metallic block is incorporated to suppress energy leakage into undesired regions. By precisely tuning the dimensions of the rectangular slot, $l_{slot} \times w_{slot}$ (422 µm $\times$ 422 µm in this design), the transition across the three layers is optimized, allowing fine control over both phase and magnitude at the three output ports relative to the input.

The input port, located on the right side of Figure 10, is excited with a TE_{10} mode. The rectangular slot enables the division of the incident EM wave into three separate layers, each supporting a TE_{10} mode, as illustrated by the simulated E-field distribution in Figure 10b at 210 GHz.

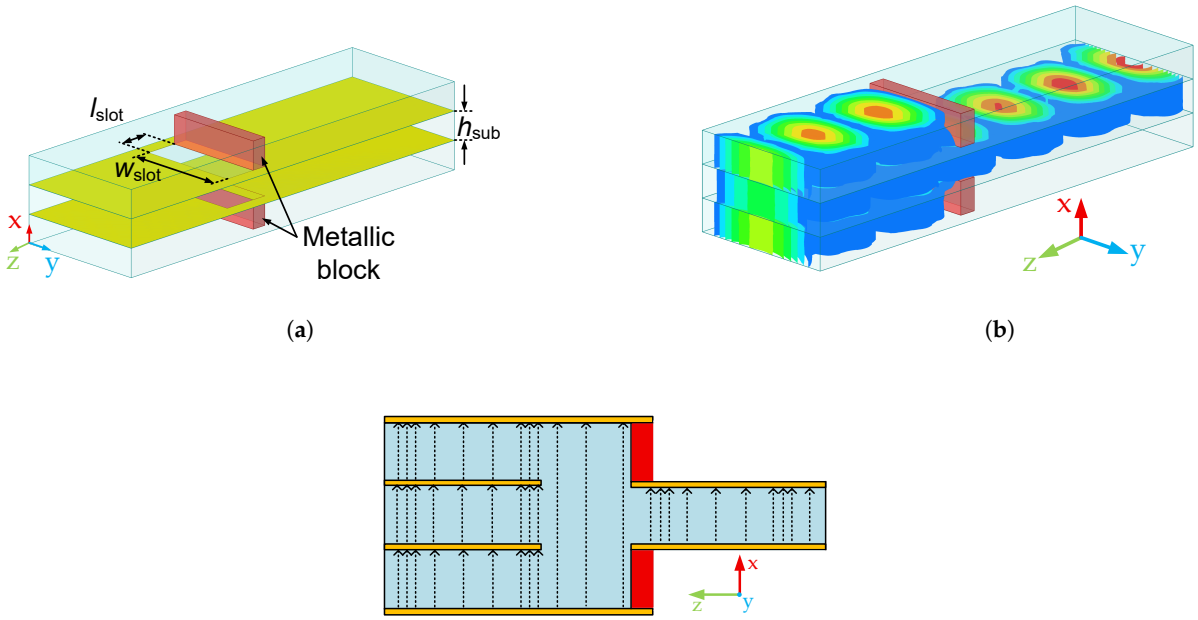

(**a**) (**b**)

(**c**)

Figure 10. Internal structure of the [a–b] section of the SIW power splitter, excluding outer conductors and vias. (**a**) Perspective view; (**b**) E-field distribution showing 1-to-3 power transition with TE_{10} mode at output ports; (**c**) Conceptual E-field lines.

4.2. [a–c] Section

In Figure 11, the wave is divided into two layers by the component in section [a–c]. The simulated E-field distribution at 210 GHz, presented in Figure 11b, demonstrates levels below −10 dB across the observed region. This section serves as the primary interface with the SIW stacked horn antenna. It features the same rectangular slot dimensions as in the [a–b] section to achieve a magnitude of $\sigma = 1.2$ and uniform phase across the outputs.

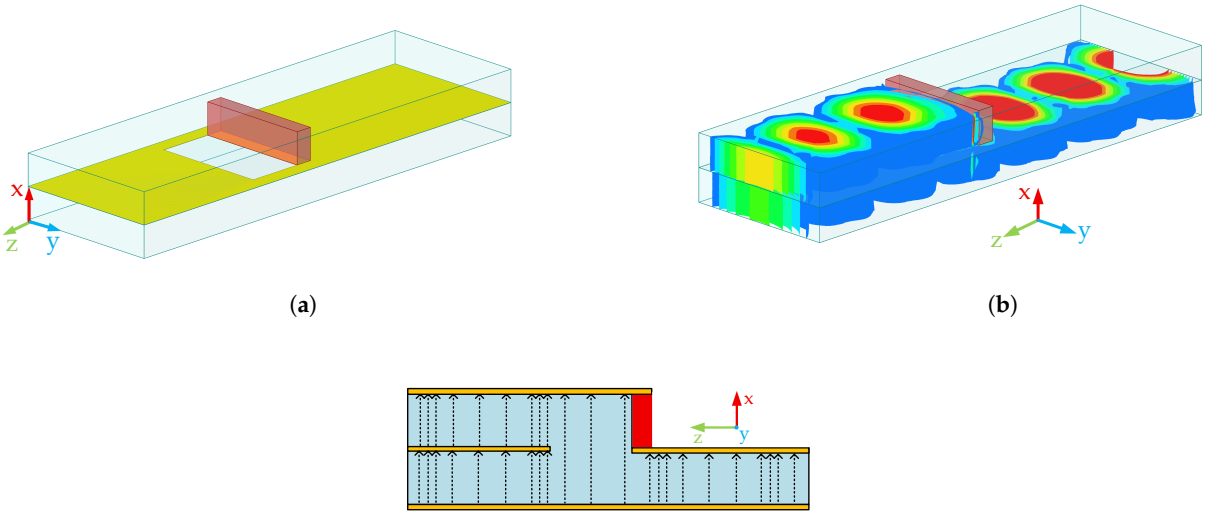

(**a**) (**b**)

(**c**)

Figure 11. Internal structure of the [a–c] section of the SIW power splitter, excluding outer conductors and vias. (**a**) Perspective view; (**b**) E-field distribution showing 1-to-2 power transition with TE_{10} mode at output ports; (**c**) conceptual E-field lines.

4.3. Complete SIW Power Splitter

The complete structure of the SIW power splitter, along with its E-field distribution and S-parameters for the overall splitter, is shown in Figure 12. This multi-layer network serves as the feeding structure for the SIW-based antenna. Ideally, the proposed divider suppresses higher-order modes and achieves equal power division across all output ports. In practice, slight amplitude variation can occur due to unequal electrical path lengths or minor impedance mismatches within the internal sections.

By tuning the dimensions of Slot I and Slot II (identical owing to the feeding network symmetry) in the [a–b] and [a–c] sections, power balance among the ports is optimized at the target frequency. Both slots maintain identical geometry to preserve phase symmetry, and the excitation magnitudes follow a Gaussian-like distribution. At 210 GHz, as illustrated in Figure 12c the input port (Port 6) exhibits a reflection coefficient below −10 dB. The transmitted powers to Ports 1 and 5 are equal, and likewise for Ports 2 and 4, demonstrating symmetrical power division across the structure. Port 3 exhibits a power level approximately 3 dB higher than Ports 2 and 4 and about 1 dB lower than Ports 1 and 5. These results closely follow the designed Gaussian amplitude taper ($\sigma = 1.2$) and are summarized in Table 2.

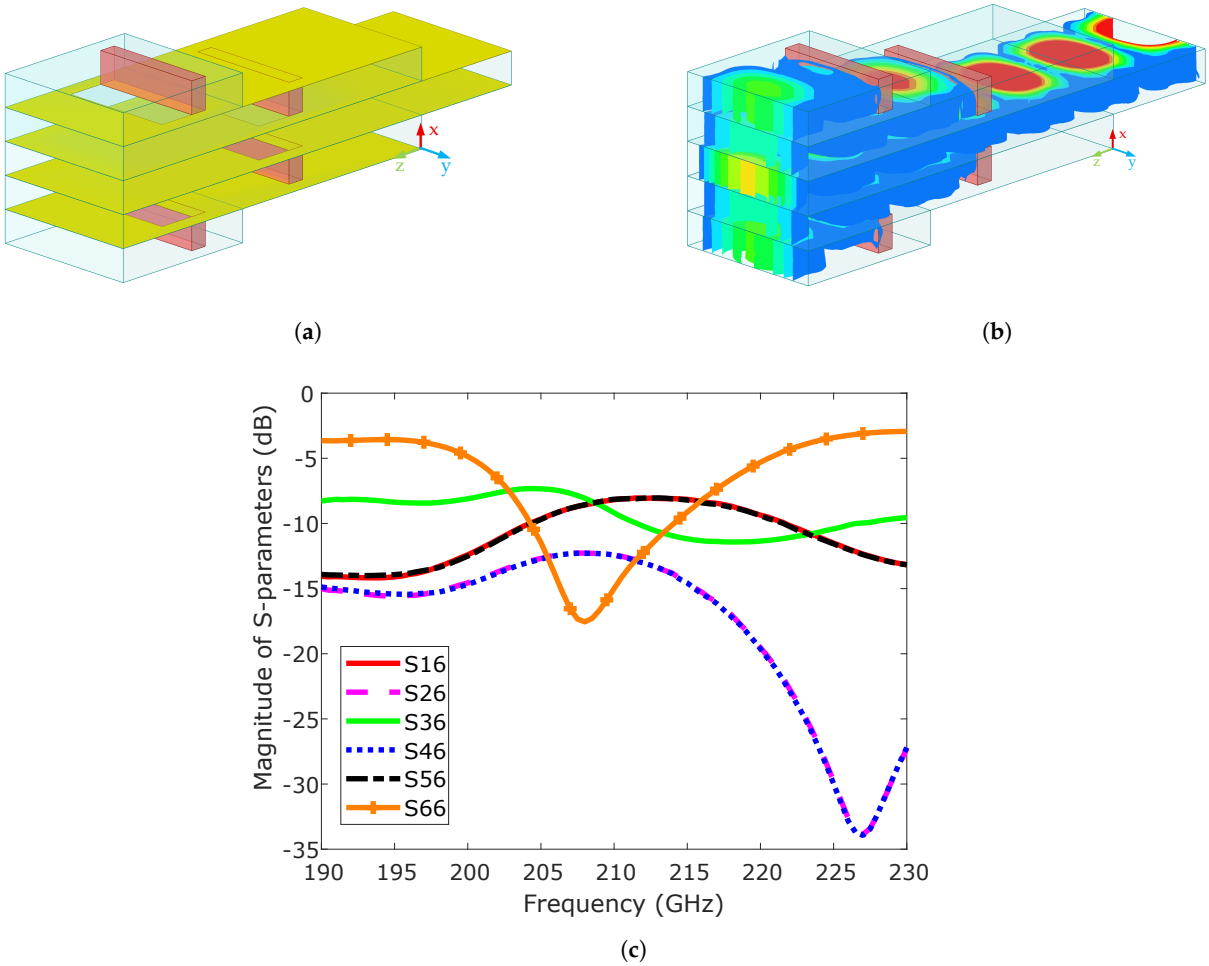

Figure 12. Complete SIW power-splitter network: (**a**) Perspective view, (**b**) E-field distribution showing 1-to-5 power transition, and (**c**) simulated S-parameters.

Figure 13a shows the simulated S-parameter magnitude as a function of slot size at 210 GHz. At a slot dimension of 422 µm × 422 µm, the magnitudes are very close to the target value of $\sigma = 1.2$, with only slight deviation observed at Ports 1 and 5. Likewise, the phase difference between all ports, shown in Figure 13b, is less than 4°. To further

evaluate fabrication tolerance, the slot dimensions were varied by ±20 µm around the nominal value. The results illustrated in Figure 13a,b, show that moderate deviations in slot size or alignment (5%) introduce less than 0.15 dB variation in coupling magnitude and below 5° phase imbalance across all ports, which are preserved within typical LTCC and PCB fabrication tolerances.

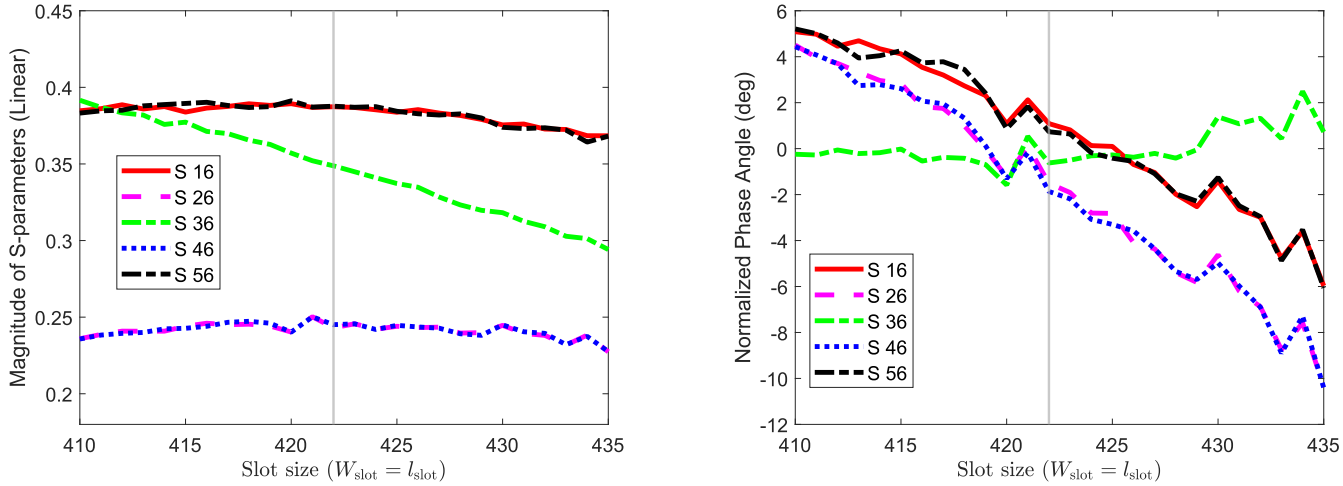

(**a**) (**b**)

Figure 13. Simulated performance of feeding network operating at 210 GHz (**a**) $|S_{n6}|$ versus slot size (**b**) Phase versus slot size.

The simulated amplitudes at the nominal slot dimension of 422 µm × 422 µm were normalized with respect to the central port (Port 3 = 1.0) and compared with the theoretical Gaussian distribution for $\sigma = 1.2$, as summarized in Table 2. While Table 2 shows our target amplitude distribution following a Gaussian taper, the full-wave EM simulation results reveal a slightly flattened profile at the outermost ports. This deviation is primarily due to edge-port truncation and boundary discontinuities at port 1 and port 5 [29]. The two distributions (theoretical and simulated) exhibit strong agreement, with deviations within ±10%, confirming that the proposed slot-coupled feeding network accurately reproduces the desired Gaussian taper across the five stacked ports. Therefore, the proposed feeding network demonstrates strong robustness against practical manufacturing variations, ensuring stable excitation for THz implementations.

Table 2. Comparison of theoretical Gaussian and simulated normalized magnitudes at 210 GHz ($\sigma = 1.2$, normalized to Port 3 = 1.0, slot dimension = 422 µm × 422 µm)

Port	Theoretical Gaussian	Simulated Normalized Magnitude
1	0.25	1.13
2	0.80	0.70
3	1.0	1.0
4	0.80	0.72
5	0.25	1.13

5. SIW Horn Antenna Fed by Complete SIW Power Splitter

The S-parameter of the complete antenna fed through a single port is shown in Figure 14a. It clearly shows a resonance at 210 GHz, with an $|S_{66}|$ value of less than –10 dB, indicating good impedance matching at the operating frequency. Figure 14b,c present

the 3D radiation pattern (gain) and co- and cross-polarization for both E- and H-planes, respectively, at 210 GHz, demonstrating a peak gain of approximately 10 dB.

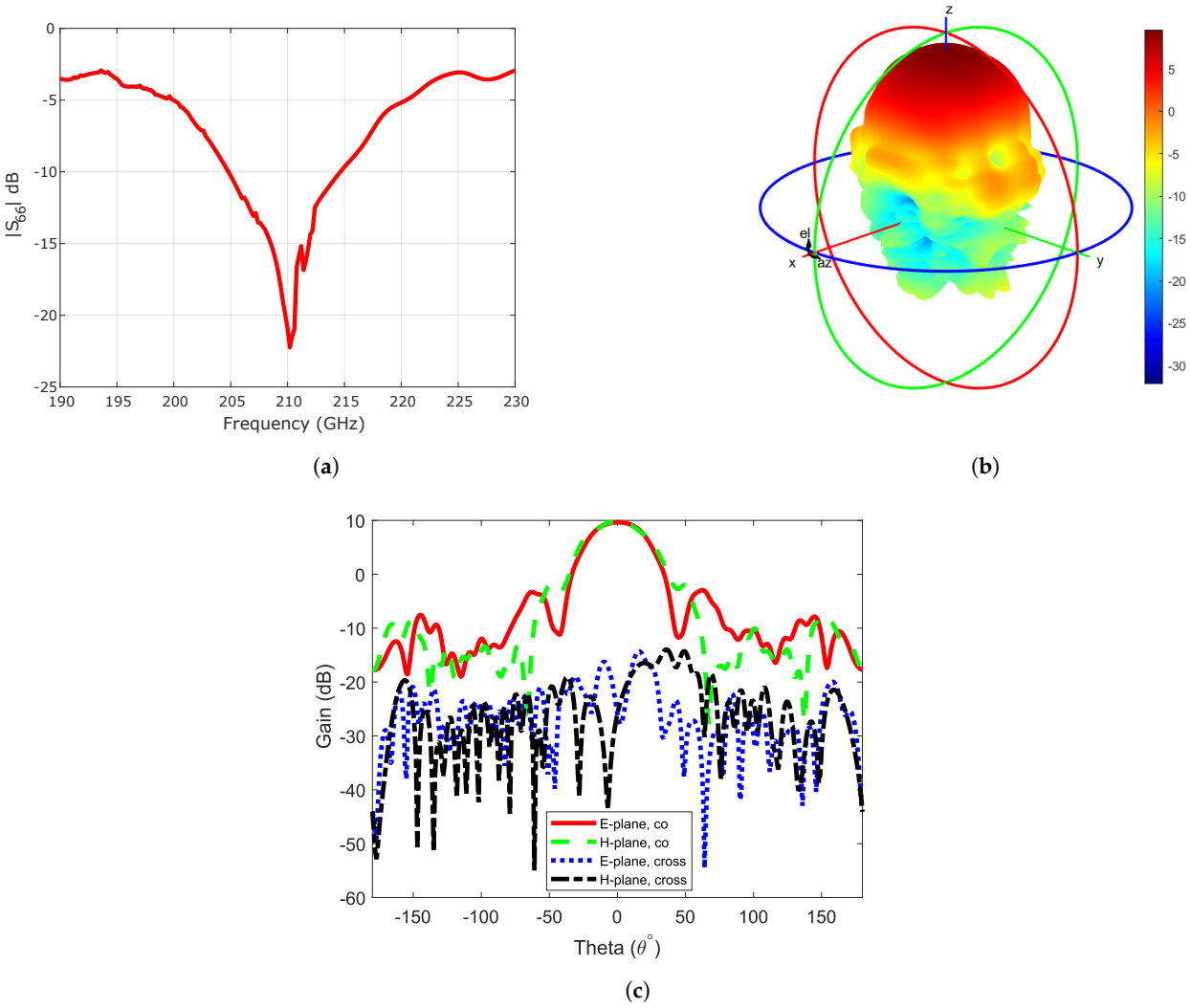

Figure 14. Simulated result of the complete SIW horn antenna feed by the feeding network (**a**) S-parameter $|S_{66}|$, (**b**) 3D radiation pattern (Gain), and (**c**) co- and cross-polarization at 210 GHz.

The overall antenna efficiency was evaluated to assess the performance of the stacked SIW horn at the operating frequency. At 210 GHz, the simulated radiation efficiency is 50.3%. This moderate efficiency is consistent with expectations for THz-band antennas using polymer dielectrics: low-loss polymers like polyimide exhibit non-zero loss tangents at millimetre-wave and THz frequencies [30,31]. The efficiency is primarily limited by dielectric loss, conductor (metal) loss, and the increased path length through the stacked layers.

The E- and H-plane gain cuts for the direct excitation and via the SIW feed-line are shown in Figure 15a,b. Figure 15c plots the differential in gain between via SIW feed-line and direct excitation. For $\theta \approx 41^\circ$ in both planes, the difference is closer to 0 dB, confirming that the feed-line preserves the main beam (gain and HPBW). Beyond this range, the E-plane exhibits larger excursions of ΔG, whereas the H-plane remains comparatively stable. This behaviour is consistent with a small amplitude imbalance at the feed network's outer ports (Port 1/ Port 5), primarily affecting the E-plane SLLs. All the simulations were conducted at 210 GHz.

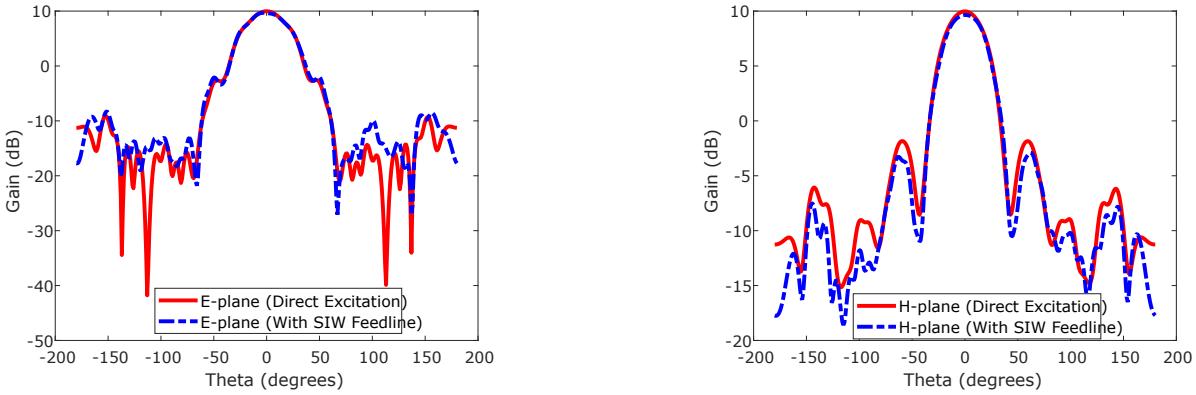

(**a**) (**b**)

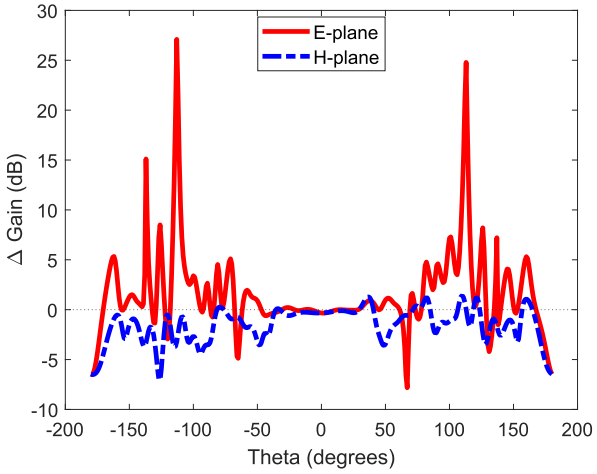

(**c**)

Figure 15. Comparison of radiation pattern between direct excitation and through SIW feeding network (**a**) E-Plane, (**b**) H-plane, and (**c**) Differential plot ($\Delta G(\theta) = G_{\text{feedline}}(\theta) - G_{\text{direct}}(\theta)$).

The E-field distribution of the complete SIW horn antenna, fed by the SIW feeding network, is shown in Figure 16. The antenna is excited through a single input port, which is progressively split into five layers via etched slots to achieve the required excitation magnitudes and phase values. The first slot (Slot I) divides the EM signal into three parts, while the second slot (Slot II) further splits it into two parts. The phase and magnitude at each output are controlled by the dimensions of the slots. As the wave propagates, the energy is distributed among the five layers, gradually reducing the field intensity. The remaining sections of the horn and the dielectric loading act as a lens, focusing the EM wave in the end-fire direction.

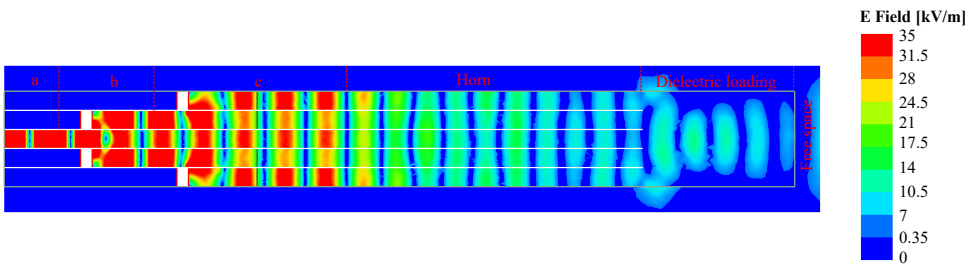

Figure 16. E-plane view of E-field distribution of the complete SIW horn antenna feed with SIW feeding network at 210 GHz.

The proposed stacked SIW-based pyramidal horn antenna, operating at 210 GHz, is well-suited for non-invasive imaging systems, high-resolution imaging, and short-range high-capacity wireless communications. THz frequencies have a large accessible bandwidth, which makes them perfect for 6G front and backhaul applications and ultra-high-speed wireless backhaul, where directive beams can compensate for significant atmospheric attenuation [32,33]. Furthermore, the antenna can accommodate radar-type integrated sensing and communication (ISAC) platforms [16], with minor feeding network modification such as tight inter-port phase balance, small phase shifter for steering and shaping [34], duplexing with right radome, and stronger amplitude taper for lower SLL.

Although fabrication tolerances have been considered in this study, practical measurement of THz SIW antennas introduces additional challenges that may lead to deviations from the simulated performance. At 210 GHz, probe-based excitation is highly sensitive to probe-to-port alignment, and small misalignment, particularly in the E-plane, which can significantly degrade coupling and introduce phase imbalance [35]. Moreover, the repeated calibration and de-embedding procedures for fixtures and transitions at sub-THz frequencies are nontrivial; residual parasitic and calibration uncertainty can distort the measured response [36]. Variations in dielectric properties, loss tangent, and surface roughness (especially of metallic surfaces) at these frequencies further contribute to measurement error, potentially causing frequency shifts and lowering measured gain [37]. In antenna far-field characterization, mechanical tolerances, positioning accuracy, and chamber reflections are known sources of error, particularly at short wavelengths [38]. These combined effects may result in a modest reduction in gain, slight broadening or asymmetry of the HPBW, and increased SLLs relative to simulation. A comparison of the proposed antenna with other reported THz horn antennas is presented in Table 3, highlighting its performance in terms of bandwidth, gain, and beamwidths.

Table 3. Comparison between the proposed SIW horn antenna and other reported THz horn antennas.

Reference	Feeding Mechanism	Operating Frequency (GHz)	Bandwidth (GHz)	Max. Gain (dBi)	Beamwidths (E/H, °)	Overall Geometry
[2]	Effective-medium dielectric waveguide with taper feed	220–330	110	11.2–15.0	20 / 85	flare section = 2.88 mm ($\theta \approx 60°$); 1.39 mm lens; total geometry $7.27 \times 3.40 \times 0.25$ mm^3
[3]	Four vertically stacked TE_{10} SIW ports with phase & amplitude correction network	35	16	13.1	33 / 33	Rogers 5880 ($\epsilon_r = 2.2, \tan\delta = 0.0009$, total height = 12.6 mm); H-plane flare angle 34°
[4]	Dual-port stacked SIW structure with sloping-slot coupling to excite TE_{01} mode	17.6–19.8	17–22	8.1–10.3	40 / 40	substrate ($\epsilon_r = 2.2, \tan\delta = 0.001$, thickness = 4.3 mm); slot/horn length = 25.7/24 mm; flare angle = 20°; feeding width = 10.6 mm
[5]	Horizontal & vertical power dividers	135–145	9	13.3	34 / 16	Ferro A6-M substrate ($\epsilon_r = 5.9, \tan\delta = 0.001$, thickness = 0.09652 mm); horn width/length/height = 2.8/3.2/0.77 mm

Table 3. *Cont.*

Reference	Feeding Mechanism	Operating Frequency (GHz)	Bandwidth (GHz)	Max. Gain (dBi)	Beamwidths (E/H, °)	Overall Geometry
[6]	Coaxial probe-fed H-plane SIW horn	12.9–18	34%	8.5–11.0	40 / 40	Roger Rt/Duroid 5880 substrate ($\epsilon_r = 2.2$, height = 1.57 mm) optimized dimensions $48.1 \times 31 \times 4.11$ mm^3
[39]	E/H plane corporate SIW feeding network	35–41	6	15.8–23.8	12 / 40	horn width ≈ 5.6 mm; E-plane = 4.9 mm; total stack height ≈ 12.2 mm
This work	Five-port TE_{10} SIW feeding network	210	10	10.0	41 / 41	Polyimide ($\epsilon_r = 3.5, \tan\delta = 0.008$, thickness = 1.25); flare angle 60°; dielectric lens = 1.25 mm

6. Conclusions

This work presented a stacked SIW-based pyramidal horn antenna for THz band applications, designed to achieve equal HPBWs in both the E- and H-planes through a five-layer dielectric-loaded configuration. By employing optimized slot apertures and a matched TE_{10}-mode feeding network, the antenna achieves efficient vertical power transfer, minimal reflection, and high mode purity. Full-wave simulations confirm a gain of 10 dBi, HPBW of 41°, and sidelobe levels around −3.2 dB in both planes. The study emphasizes a simulation-driven design methodology that explores the influence of geometric, material, and excitation parameters within the limits of practical LTCC and PCB fabrication processes.

Although the antenna has not yet been fabricated or experimentally tested due to insufficient budget to access overseas foundry and testing facilities, we have made every effort to provide comprehensive results. All simulated dimensions and tolerances were selected to reflect realistic, manufacturable constraints achievable with commercially available multilayer SIW processes, and the design was developed to be fabrication-ready. Future work will involve collaborative fabrication and experimental validation with institutions equipped for sub-THz prototyping. The proposed antenna concept establishes a robust and fabrication-ready framework for compact, high-performance, and beam-symmetric antennas for THz communication and sensing applications.

Author Contributions: Conceptualization, B.P.; Methodology, B.P.; Validation, B.P., X.J.L.; Formal analysis, B.P., X.J.L.; Investigation, B.P.; Writing—original draft, B.P.; Writing—review & editing, X.J.L. and B.-C.S.; Supervision, X.J.L. and B.-C.S. All authors have read and agreed to the published version of the manuscript.

Funding: This research received no external funding.

Data Availability Statement: All the data are available within the manuscript.

Conflicts of Interest: The authors declare no conflicts of interest.

Appendix A. Peak Gain Values as Functions of Antenna Design Parameter

In this section, we illustrate the peak gain plot as a function of antenna design parameters like the number of dielectric layers, the length of dielectric loading, different taper σ values, and phase difference $\Delta\phi$.

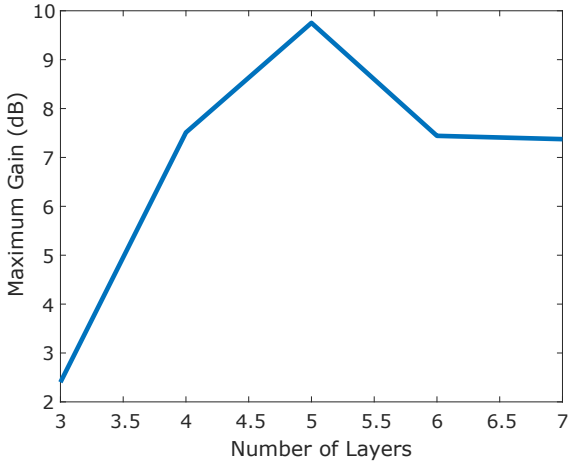

(**a**)

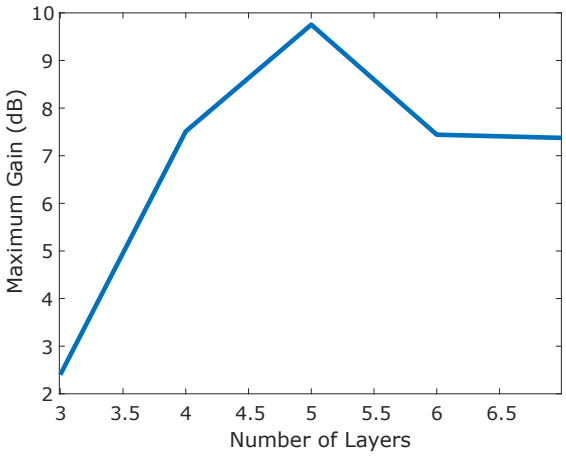

(**b**)

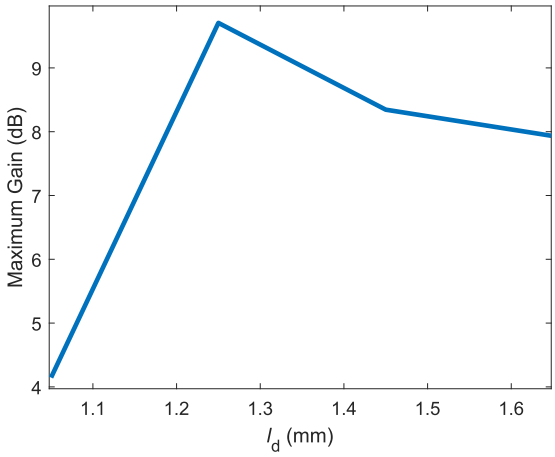

(**c**)

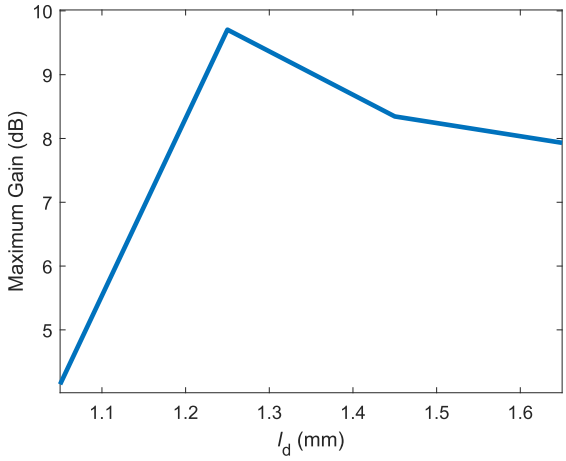

(**d**)

Figure A1. Peak gain of the proposed SIW stacked horn antenna for different design parameters. (**a**) E-plane and (**b**) H-plane for varying number of stacked SIW layers. (**c**) E-plane and (**d**) H-plane for varying dielectric loading lengths.

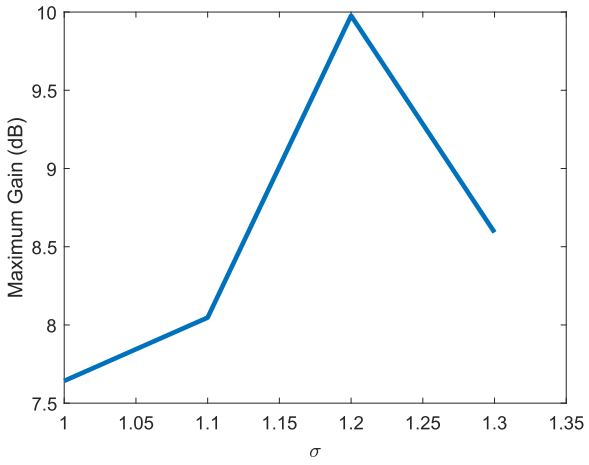

(**a**)

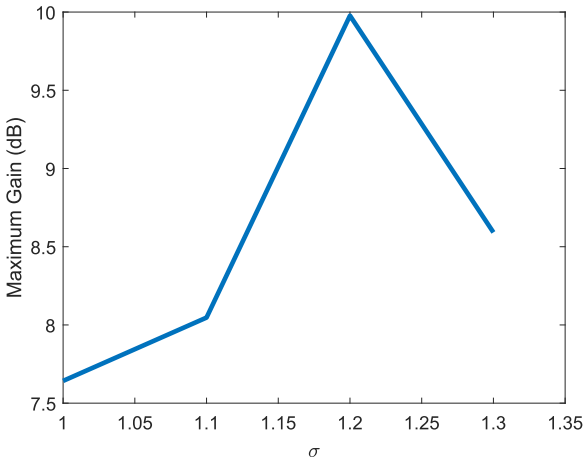

(**b**)

Figure A2. *Cont.*

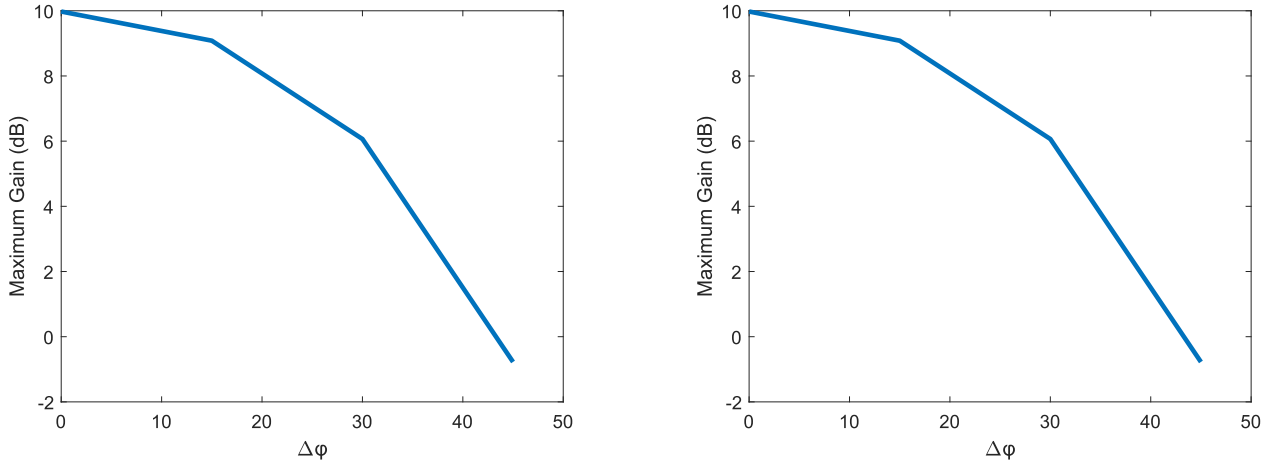

(**c**) (**d**)

Figure A2. Peak gain of the proposed SIW stacked horn antenna for different design parameters. (**a**) E-plane and (**b**) H-plane for varying number of taper magnitude (σ). (**c**) E-plane and (**d**) H-plane for varying phase difference ($\Delta\phi$).

References

1. Lin, T.Y.; Lin, S.G.; Chang, Y.C.; Hsieh, C.; Chang, D.C. A broadband sub-THz band stacked transition of SIW-to-SIW. In Proceedings of the 2023 IEEE 27th Workshop on Signal and Power Integrity (SPI), Aveiro, Portugal, 7–10 May 2023; pp. 1–2.
2. Liang, J.; Gao, W.; Lees, H.; Withayachumnankul, W. All-silicon terahertz planar horn antenna. *IEEE Antennas Wirel. Propag. Lett.* **2021**, *20*, 2181–2185. [CrossRef]
3. Gong, L.; Fu, Y.; Chan, K.Y.; Nanzer, J.A.; Ramer, R. An SIW horn antenna fed by a coupled mode emulating pyramidal horn antennas. *IEEE Trans. Antennas Propag.* **2019**, *68*, 33–42. [CrossRef]
4. Cai, Y.; Zhang, Y.; Qian, Z.; Cao, W.; Shi, S. Compact wideband dual circularly polarized substrate integrated waveguide horn antenna. *IEEE Trans. Antennas Propag.* **2016**, *64*, 3184–3189. [CrossRef]
5. Yeap, S.B.; Qing, X.; Sun, M.; Chen, Z.N. 140-GHz 2×2 SIW horn array on LTCC. In Proceedings of the 2012 IEEE Asia-Pacific Conference on Antennas and Propagation, Singapore, 27–29 August 2012; pp. 279–280.
6. Sahoo, S.K.; Adhikary, M.; Biswas, A.; Akhtar, M.J. Multi-layer multi-dielectric lens loaded SIW horn antenna for Ku-band applications. In Proceedings of the 2021 15th European Conference on Antennas and Propagation (EuCAP), Düsseldorf, German, 22–26 March 2021; pp. 1–5.
7. Li, Z.; Wu, K.; Denidni, T.A. A new approach to integrated horn antenna. In Proceedings of the 2004 10th International Symposium on Antenna Technology and Applied Electromagnetics and URSI Conference, Pisa, Italy, 23–27 May 2004; pp. 1–3.
8. Paudel, B.; Li, X.J.; Seet, B.C. Rectangular Waveguide TE_{10} to Substrate Integrated Waveguide TE_{20} Probe-less Mode Converter for Planar Terahertz Applications. In Proceedings of the 2025 6th Australian Microwave Symposium (AMS), Gold Coast, Australia, 10–11 February 2025; pp. 1–2.
9. Paudel, B.; Li, X.J.; Seet, B.C. A Broadband Mode Converter Antenna for Terahertz Communications. *Electronics* **2025**, *14*, 551. [CrossRef]
10. Esquius-Morote, M.; Fuchs, B.; Zürcher, J.F.; Mosig, J.R. A printed transition for matching improvement of SIW horn antennas. *IEEE Trans. Antennas Propag.* **2012**, *61*, 1923–1930. [CrossRef]
11. Xie, Z.; Liu, B.; Zhao, Y.; Tian, B.; Jia, S. A novel Ka band multi-layer SIW power divider. In Proceedings of the 2011 Cross Strait Quad-Regional Radio Science and Wireless Technology Conference, Harbin, China, 26–30 July 2011; Volume 1, pp. 634–636.
12. Zhou, Y.; Song, K.; Guo, S.; Li, Q.; Aidoo, M.W.; Fan, Y. Novel subterahertz high isolation stacked-SIW power divider. *IEEE Trans. Terahertz Sci. Technol.* **2023**, *13*, 316–323. [CrossRef]
13. Ettorre, M.; Sauleau, R.; Le Coq, L. Multi-beam multi-layer leaky-wave SIW pillbox antenna for millimeter-wave applications. *IEEE Trans. Antennas Propag.* **2011**, *59*, 1093–1100. [CrossRef]
14. Wang, S.; Chung, K.L.; Du, L.; Kong, F.; Li, K. Design and analysis of a compact frequency beam-scanning antenna based on composite FHMSIW/SSPP waveguide. *IEEE Antennas Wirel. Propag. Lett.* **2021**, *21*, 546–550. [CrossRef]
15. Nagatsuma, T.; Ducournau, G.; Renaud, C.C. Advances in terahertz communications accelerated by photonics. *Nat. Photonics* **2016**, *10*, 371–379. [CrossRef]
16. Elbir, A.M.; Mishra, K.V.; Chatzinotas, S.; Bennis, M. Terahertz-band integrated sensing and communications: Challenges and opportunities. *IEEE Aerosp. Electron. Syst. Mag.* **2024**, *39*, 38–49. [CrossRef]

17. Han, C.; Yan, L.; Yuan, J. Hybrid beamforming for terahertz wireless communications: Challenges, architectures, and open problems. *IEEE Wirel. Commun.* **2021**, *28*, 198–204. [CrossRef]
18. Shi, M.; Wu, Q.; Yu, C.; Wang, H.; Hong, W. Broadband center-fed SIW slot array antenna with multi-layer transition for 79 GHz automotive radar. In Proceedings of the 2019 International Symposium on Antennas and Propagation (ISAP), Xi'an, China, 27–30 October 2019; pp. 1–3.
19. Zou, X.; Fan, Y.; Zhang, D.; Chen, Q.; Qian, H. SIW Transition Structure of Double-layer Substrates and Its Application in 3dB Coupler. In Proceedings of the 2024 Photonics & Electromagnetics Research Symposium (PIERS), Chengdu, China, 21–25 April 2024; pp. 1–8.
20. Wang, L.; Garcia-Vigueras, M.; Alvarez-Folgueiras, M.; Mosig, J.R. Wideband H-plane dielectric horn antenna. *IET Microwaves Antennas Propag.* **2017**, *11*, 1695–1701. [CrossRef]
21. Wu, K.; Deslandes, D.; Cassivi, Y. The substrate integrated circuits—A new concept for high-frequency electronics and optoelectronics. In Proceedings of the 6th International Conference on Telecommunications in Modern Satellite, Cable and Broadcasting Service, 2003, TELSIKS 2003, Nis, Serbia, 1–3 October 2003; Volume 1, pp. P–III.
22. Pozar, D.M. The active element pattern. *IEEE Trans. Antennas Propag.* **2002**, *42*, 1176–1178. [CrossRef]
23. Nakano, H.; Iwatsuki, M.; Sakurai, M.; Yamauchi, J. A cavity-backed rectangular aperture antenna with application to a tilted fan beam array antenna. *IEEE Trans. Antennas Propag.* **2003**, *51*, 712–718. [CrossRef]
24. Vosoogh, A.; Kildal, P.S. Simple formula for aperture efficiency reduction due to grating lobes in planar phased arrays. *IEEE Trans. Antennas Propag.* **2016**, *64*, 2263–2269. [CrossRef]
25. Wang, H.; Fang, D.G.; Zhang, B.; Che, W.Q. Dielectric loaded substrate integrated waveguide (SIW) *H*-plane horn antennas. *IEEE Trans. Antennas Propag.* **2009**, *58*, 640–647. [CrossRef]
26. Ahmed, M.F.; Haraz, O.M.; Kaddoum, G.; Alshebili, S.A.; Sebak, A.R. On using Gaussian excitation amplitudes to improve the antenna array radiation characteristics. In Proceedings of the 2014 IEEE Asia-Pacific Conference on Applied Electromagnetics (APACE), Johor Bahru, Malaysia, 8–10 December 2014; pp. 131–134.
27. Balanis, C.A. *Antenna Theory: Analysis and Design*; John Wiley & Sons: Hoboken, NJ, USA, 2016.
28. Kordiboroujeni, Z.; Bornemann, J. Designing the width of substrate integrated waveguide structures. *IEEE Microw. Wirel. Components Lett.* **2013**, *23*, 518–520. [CrossRef]
29. Karimi, A.; Oberhammer, J. Design of an amplitude-tapered corporate-feed slot array antenna with reduced side-lobe level for silicon micromachining. In Proceedings of the 2022 16th European Conference on Antennas and Propagation (EuCAP), Madrid, Spain, 27 March–1 April 2022; pp. 1–5.
30. Carter, J.; Lees, H.; Wang, Q.; Chen, S.J.; Atakaramians, S.; Withayachumnakul, W. Terahertz properties of common microwave dielectric materials. *J. Infrared Millim. Terahertz Waves* **2023**, *44*, 873–884. [CrossRef]
31. Sahin, S.; Nahar, N.K.; Sertel, K. Dielectric properties of low-loss polymers for mmW and THz applications. *J. Infrared Millim. Terahertz Waves* **2019**, *40*, 557–573. [CrossRef]
32. Paudel, B.; Li, X.J.; Seet, B.C. Design and modeling of a terahertz transceiver for intra-and inter-chip communications in wireless network-on-chip architectures. *Sensors* **2024**, *24*, 3220. [CrossRef]
33. Braun, R.P.; Schneider, T. Propagation of Millimeter-Wave Fixed Wireless Backhaul/Fronthaul. In *Handbook of Radio and Optical Networks Convergence*; Springer: Berlin/Heidelberg, Germany, 2023; pp. 1–18.
34. van Berkel, S.; Khanal, S.; Rahiminejad, S.; Jung-Kubiak, C.; Maestrini, A.E.; Chattopadhyay, G. MEMS Phase Shifters for THz Beam-Scanning: Demonstration with a 500–600 GHz Phased Array with Leaky-Wave Feeds. *IEEE Trans. Terahertz Sci. Technol.* **2024**, *14*, 830–842. [CrossRef]
35. Jayasankar, D.; Koj, A.; Hesler, J.; Stake, J. Impact of E-plane Misalignment on THz Diagonal Horn Antennas. *IEEE Trans. Terahertz Sci. Technol.* **2024**, *15*, 143–150. [CrossRef]
36. Rumiantsev, A.; Swe, T.N.; Henkel, A. Achieving Metrology-Level Accuracy When Making THz Measurements. *Microw. J.* **2016**, *59*, 140.
37. Kazemipour, A.; Wollensack, M.; Hoffmann, J.; Hudlička, M.; Yee, S.K.; Rüfenacht, J.; Stalder, D.; Gäumann, G.; Zeier, M. Analytical uncertainty evaluation of material parameter measurements at THz frequencies. *J. Infrared Millim. Terahertz Waves* **2020**, *41*, 1199–1217. [CrossRef]
38. Le Coq, L.; Mézières, N.; Leroy, P.; Fuchs, B. Some contributions for antenna 3d far field characterization at terahertz. *Sensors* **2021**, *21*, 1438. [CrossRef]
39. Segura-Gómez, C.; Palomares-Caballero, A.; Padilla, P. A 1-to-8 fully modular stacked SIW antenna array for millimeter-wave applications. *IEEE Trans. Antennas Propag.* **2022**, *70*, 11149–11154. [CrossRef]